AIAA JOURNAL
Vol. 38, No. 11, November 2000

Unsteady Flow Computations of a Slat with a Blunt Trailing Edge

Mehdi R. Khorrami,* Mert E. Berkman,† and Meelan Choudhari‡
High Technology Corporation, Hampton, Virginia 23666

A detailed computational study of a high-lift configuration was conducted to understand the source mechanism behind a dominant acoustic tone observed in recent experiments on slat noise. The unsteady Reynolds-averaged Navier–Stokes computations focused on accurate simulation of the local flowfield of a slat with a blunt trailing edge. At a slat deflection angle of 30 deg relative to the main element, the simulations revealed the presence of strong vortex shedding behind the slat trailing edge. The resulting flow unsteadiness produced large-amplitude acoustic waves propagating away from the trailing-edge region. The local spatial resolution of the computed solution was sufficiently fine to capture both the near-field structure and propagation direction of the generated sound. The calculated shedding frequency is in good agreement with the measured acoustic frequencies obtained at NASA Langley Research Center's Low Turbulence Pressure Tunnel. In contrast, computational results at a slat deflection angle of 20 deg indicated that the shedding process was severely damped, and, therefore, in agreement with the corresponding acoustic measurements during the experiment. There was no evidence of a strong acoustic source near the trailing edge at this lower slat deflection.

I. Introduction

VARIOUS components of the airframe are known to be a significant source of noise. In the past, understanding and reducing airframe-generated noise did not receive much focused attention. With the significant quieting of modern, high-bypass-ratioturbofan engines, airframe noise now competes with engine noise and, in certain instances, even surpasses it. Airframe noise is most pronounced during aircraft approach and landing, when the engines are operating at reduced thrust and airframe components such as high-lift devices and landing gears are in deployed condition. Future Federal Aviation Administration noise regulations will require the fleet of civil transport to be substantially quieter than currently operational aircraft. With the worldwide increase in population density near major airports and the projected growth in air travel, imposition of even more stringent noise regulations is imminent. Consequently, the study of airframe noise has become an important research topic.

Recent experimental studies in both the United States and Europe (e.g., Refs. 1–4) have highlighted and reaffirmed the role of high-lift devices as the dominant contributors to airframe noise in the mid- to high-frequency range. In particular, the most significant sources of noise have been identified with the leading-edge slat and the side edges of the flaps. Therefore, a concerted effort toward understanding the slat and flap side-edge flowfields and their acoustic characteristics is currently underway as part of NASA's Advanced Subsonic Technology (AST) program. Initially, the extensive computational and experimental efforts were directed at delineating the precise noise source mechanisms near a flap side edge.[1,5–12] More recently, attention has been focused on noise sources involving the slat. To accomplish this task, a generic energy efficient transport (EET) high-lift configuration was tested in the Low Turbulence Pressure Tunnel (LTPT) at NASA Langley Research Center. The three-element model consisted of a slat, a main wing, and a partial-span flap (Fig. 1). Extensive aerodynamic and acoustic measurements were made during these tests.

The acoustic data was obtained using a phased microphone array by a team from The Boeing Commercial Airplane Company. The array was mounted on the LTPT ceiling, roughly 1 m above the model, which had been mounted upside down in the tunnel to mimic the flyover path (Fig. 2). The LTPT facility allows the flow Reynolds number Re to be varied while holding the Mach number M constant. The experiments were carried out at four distinct Reynolds numbers, namely, 3.6, 7.2, 14.4, and 19 ($\times 10^6$), based on the stowed chord of the three-element wing. The baseline settings employed during the tests involved a main element angle of attack of 10 deg, a flap deflection angle of 30 deg, and slat deflection angles of 30 and 20 deg, respectively.

The microphone array measurements of the EET slat for the two slat deflections are shown in Figs. 3 and 4, respectively. The displayed spectra are in $\frac{1}{12}$th-octave bands. The flow Mach number is 0.2, corresponding to a typical approach condition in practice. The following features in the slat spectra are worth noting. For the 30-deg case, the measurements show high sound levels in the lower frequency range, followed by a gradual decrease. In the vicinity of 40–50 kHz, however, the spectra display a very high-amplitude tonelike feature (hump). For certain test conditions, the sound levels associated with this peak were so high that they virtually masked any other sources of noise. At the lowest Reynolds number setting included in these tests, $Re = 3.6 \times 10^6$, the peak occurred at a slightly lower frequency ($\approx$42 kHz) and had an amplitude that was 30–50% lower than the amplitude at the largest Reynolds number, $Re = 19.0 \times 10^6$. A similar peak in the slat spectrum had also been observed in the earlier acoustic measurements of a generic high-lift system in the NASA Ames Research Center 7×10 ft tunnel.[5]

At a slat deflection of 20 deg, the sound levels are substantially lower than the 30-deg case. In particular, the tonelike hump at high frequency virtually disappears. The disappearance of the high-frequency noise source at the lower slat deflection had also been noted in the NASA Ames Research Center 7×10 experiment by Storms et al.[5] Although several mechanisms had been theorized by the members of the AST airframe noise team to explain this loud acoustic peak, no clear understanding of the underlying noise source mechanism had emerged.

The objective behind the present work was to rectify the described deficiency via unsteady flow simulation of the EET high-lift system. Specifically, our goal was to prove or disprove, via computational simulations, the conjecture that vortex shedding at the somewhat blunt slat trailing edge is the mechanism responsible for the hump at high frequencies. To that end, special attention was focused on the fine resolution and accurate computation of the important flow features in the vicinity of the slat in general and the blunt trailing edge in particular.

Received 18 October 1999; revision received 3 March 2000; accepted for publication 28 April 2000.

*Senior Scientist, 28 Research Drive. Senior Member AIAA.
†Research Scientist, 28 Research Drive. Member AIAA.
‡Senior Research Scientist; currently Research Scientist, Computational Modeling and Simulations Branch, NASA Langley Research Center, Hampton, VA 23681-2199. Senior Member AIAA.

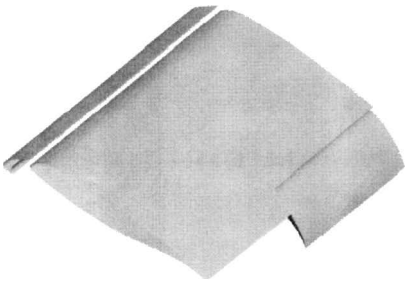

a) Three-dimensional model

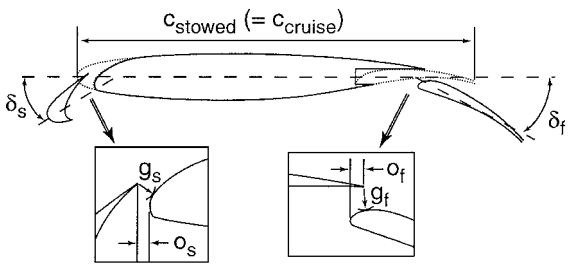

b) Cross-sectional view

Fig. 1 Three-element EET high-lift system.

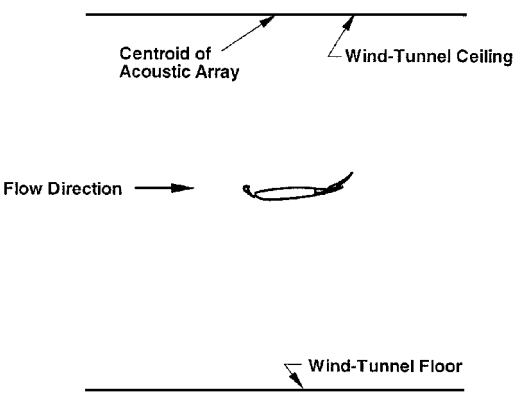

Fig. 2 Schematic of model setup in tunnel for acoustic measurements.

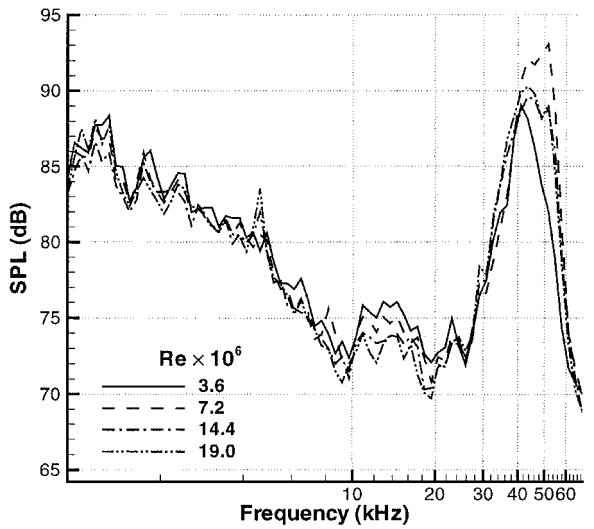

Fig. 3 Measured acoustic spectra for slat in $\frac{1}{12}$th-octave bands with test parameters slat deflection angle of 30 deg, main element angle of attack 10 deg, flap deflection angle of 30 deg, and Mach number of 0.2.

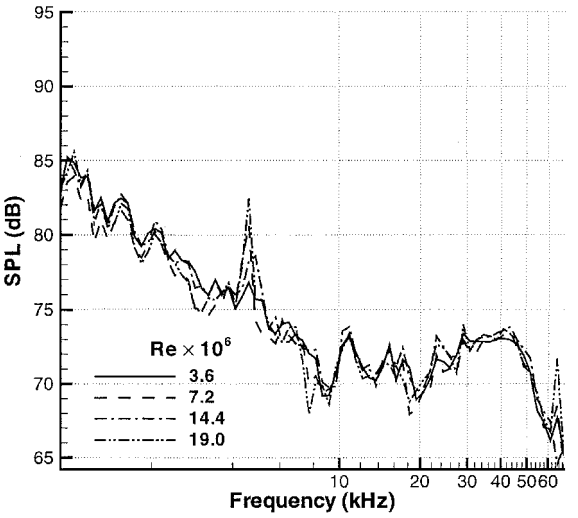

Fig. 4 Measured acoustic spectra for slat in $\frac{1}{12}$th-octave bands with test parameters slat deflection angle of 20 deg, main element angle of attack of 10 deg, flap deflection angle of 30 deg, and Mach number of 0.2.

The organization of the paper is as follows. In Sec. II, we describe the computational procedure, including an account of the model geometry, grid generation, and the flow solver used. Detailed analysis of the simulation data is presented in Sec. III, wherein we discuss the effects of varying the slat deflection angle, Reynolds number, and trailing-edge thickness, respectively, on vortex shedding characteristics. Finally, concluding remarks are presented in Sec. IV.

II. Computational Procedure

A. Flow Solver

The CFL3D code (described in detail by Thomas et al.[13]) was used to compute the flowfield. The CFL3D code solves the compressible three-dimensional, time-dependent, thin-layer Navier–Stokes equations with a finite volume formulation. The code is characteristic based, where upwind-biased spatial differencing is used for the inviscid terms, and flux limiting is used to obtain smooth solutions in regions of large flow gradients. The flux-difference-splitting method of Roe[14] is used to obtain fluxes at the cell faces. All viscous terms are centrally differenced. The code has provisions for grid sequencing, multigridding, and local time stepping to accelerate convergence to the steady state. Also, to tackle complex flow domains, the code provides for multiblock grids with various options to treat block interfaces, for example, pointwise continuous, patched grid interpolation, chimera grid interpolation, etc.[15–17]

In CFL3D, numerous turbulence models are provided, including zero-, one-, and two-equation models. Based on our extensive past experiences with various models, the two-equation shear stress transport (k–ω) model of Menter[18] was selected to be the preferred model for the present problem. Although we suspect that a significant portion of the flow over the slat upper surface may have been transitional in practice, all of the present computations were performed assuming fully turbulent flows over all three elements.

A detailed account of time-dependent formulation employed in CFL3D was recently provided by Rumsey et al.[19,20] and, thus, will not be repeated. In short, however, the time-dependent equations were solved implicitly in time, using a combination of three-factor approximate factorization with dual time-stepping method[20] that provides second-order accuracy in both space and time. Between 25 and 30 subiterations, in conjunction with three-level V-type multigrid cycles, were utilized to ensure a minimum of two orders of magnitude drop in both the mean-flow and turbulence-model residuals during each time step.

B. Geometry and Gridding Strategy

A full account of the three-element high-lift EET model has been given by Berkman et al.[21] For the present work, note that in the stowed position, the model has a chord of 21.65 in. (0.55 m) with the slat and flap chords of 15 and 30%, respectively. The important geometrical settings, that is, the gaps g_s and g_f, and the overhangs

Table 1 Geometrical settings

Parameter	Setting
Slat angle δ_s, deg	20, 30
Flap angle δ_f, deg	30
Slat gap g_s, %	2.44
Flap gap g_f, %	3.0
Slat overhang o_s, %	−1.52
Flap overhang o_f, %	1.7

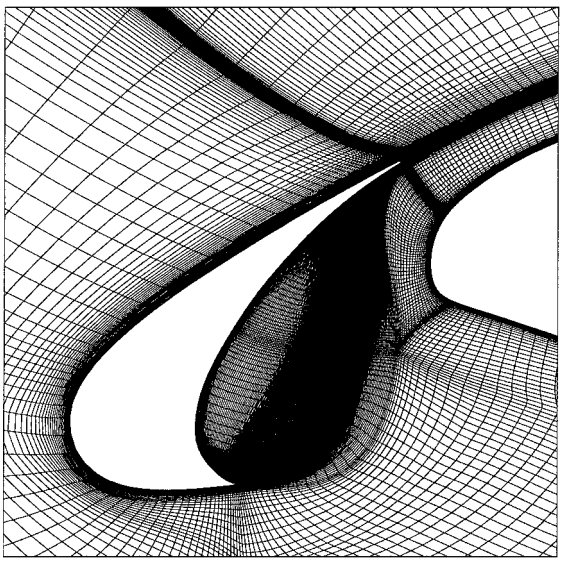

Fig. 5 Grid distribution in vicinity of slat; every other point is shown.

and o_s and o_f, in the baseline experiments for both slat deflections of 20 and 30 deg are provided in Table 1, where the distances are given as percentage of the stowed chord. The slat and flap gaps and overhangs are defined as shown in Fig. 1b. During the grid-generation process, extreme care was exercised toward precisely matching these experimental settings.

Computational costs, solution turnaround time, and the fidelity of the computed solution all depend on the quality of the grid employed. A judiciously designed grid would help to minimize the number of total grid points, while achieving the proper mesh distribution and maintaining the desired level of accuracy. The CFL3D code, with its combination of multiple-block, patching, overlapping, and embedding capabilities, provides the necessary flexibility in terms of grid generation for complex geometry simulations.

For high-lift flow computations, resolution of the boundary layers adjacent to the solid surfaces is of primary importance. Naturally, the clustering of mesh points will be near the walls. Based on our past experiences with the computations of high Reynolds number flows, approximately 20–25 points are required along wall-normal direction to resolve the thickness of the boundary layer. The placement of the first point off the wall must be handled with care. In terms of wall coordinates, the first point off a surface typically should have a y^+ of less than approximately 2. For the current simulations this requirement was met by placing the first point at 5×10^{-6} chord units off the surface.

Treatment of the trailing-edge bluntness is a crucial and challenging step in the current investigation. For accurately predicting the slat's vortex shedding, the computational trailing-edge geometry must match the actual thickness rather than being idealized as a sharp edge. For the high-lift computations, of primary importance is the capturing of the slat wake and its downstream evolution. Our grid in the vicinity of the slat is shown in Fig. 5. For clarity, every other point is displayed in both directions. The computational domain surrounding the slat was divided into multiple blocks. For this grid, the mesh clustering occurs at the solid surfaces, trailing edge, wake, and the cove. The extreme concentration of mesh points in the slat cove area (showing up as a large dark zone) is deliberate and was constructed for the purpose of accurately capturing the free shear layer that forms at the sharp tip of the slat cusp region. The completed two-dimensional grid has 19 zones, with a total of 271,000 nodes and nearly two-thirds of the points clustered in the vicinity of the slat.

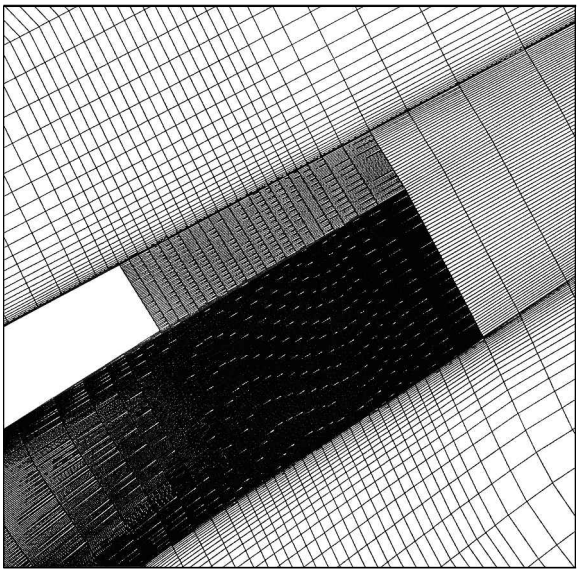

Fig. 6 Zoomed view of grid distribution at and near slat trailing edge displaying patched surface; every other point is shown.

Although the global grid picture may give the impression of a sharp trailing edge, in reality, the computational trailing-edge geometry is blunt. Two distinct values of trailing-edge thickness were employed in the present study. The first set of computations was based on a thickness h of 0.0154 in. (0.39 mm), which corresponds to the model design value. However, based on postexperimental measurements of the manufactured slat model, a thickness of 0.0196 in. (0.5 mm) was employed in the second set of computations. An enlarged view of the grid topology at the slat trailing edge is shown in Fig. 6. The fine mesh spacing (in both normal and streamwise directions) required to capture the local flow details near the trailing edge is clearly shown in Fig. 6. Within a few edge heights downstream, the fine mesh distribution is gradually relaxed to yield a sizable reduction in the overall number of grid points. For the present computations, a 1–1 matched grid block topology would propagate the dense clustering of the mesh points at the slat's trailing edge all of the way to the outflow plane and, hence, is impractical, inefficient, and not useful. The patching approach (which is supported by the CFL3D code as mentioned earlier) provides a more efficient way to handle such situations. Patching involves reducing the number of mesh points in one or two directions across a common interface shared by two adjacent grid blocks. Patched-grid interpolation is needed for communication between grids that share a common face but are not C^0 continuous. Patching works best when the grid spacing in the normal direction is approximately the same on either side of the patch interface.[22] For the slat trailing edge, the location of the patched surface can be easily identified in Fig. 6 based on a significant reduction of mesh points in the normal direction.

III. Results and Discussion

A. Steady Simulations

For purely aerodynamic results, extensive three-dimensional steady simulations of the EET high-lift system (Fig. 1) were undertaken with a grid totaling 5.6×10^6 points. Because the (slight) bluntness of the slat trailing edge is expected to have an insignificant influence on the global high-lift flowfield, all trailing edges were treated as sharp during these calculations both to minimize the required number of grid points and to facilitate solution convergence to steady state. As described by Berkman et al.,[21] the computed three-dimensional solutions showed excellent agreement with the measured mean aerodynamic quantities. To identify and capture the associated aerodynamic noise sources, an unsteady simulation of the flowfield is required. To approach the large-time behavior of the unsteady solution as efficiently as possible, it is desirable to initiate the time-accurate calculation with a flow state that is close

to the range of its final oscillatory behavior. With that in mind, the pseudostationary solution obtained after sufficiently large number of iterations based on local time stepping was used as the starting condition for time-accurate calculations.

The EET leading edge slat is two-dimensional and covers the entire model span. Previous computations[21] of the fully three-dimensional mean flow around the EET model had shown that the rapid spanwise variations associated with the downstream presence of a flap side edge are mainly localized to the vicinity of the main element trailing edge. The mean flowfield surrounding the leading edge slat was found to be essentially two dimensional, with the part-span flap reflected mainly through a modification of the overall aerodynamic loading, that is, effective angle of attack. Moreover, computational resources required to perform unsteady three-dimensional computations on a grid similar to that used in the mean-flow study are still prohibitively large at this time. For these reasons, the unsteady computations were restricted to a two-dimensional version of the high-lift geometry (Fig. 1b). The presence of the part-span flap does affect the mean circulation and, thus, loading on the leading-edge slat. To match the mean slat loading of the three-dimensional model, the current two-dimensional results were obtained with the main element at 8-deg angle of attack (as opposed to 10 deg for the experiment), which was found to yield the best match with the measured mean surface pressure distribution. All other slat and flap settings such as deflection angles, gaps, and overhangs remained identical to the experimental settings in Table 1.

The computations and postprocessing of the results were based on nondimensional flow quantities. The reference length used for nondimensionalization was the stowed chord of the three-element wing, reference speed was the speed of sound a_∞, the reference density was ρ_∞, and reference molecular viscosity was μ_∞, with the subscript ∞ denoting freestream quantities. For the present case, the reference flow variables were set to match the conditions at the entrance to the LTPT test section. As discussed earlier, the computations were done in a fully turbulent mode using the two-equation k–ω turbulence model.[18] Unless indicated otherwise, all simulations were obtained for $M = 0.2$ and $Re = 7.2 \times 10^6$.

For each individual case, the flow solver was first run in the steady mode until the residuals dropped 4–4.5 orders of magnitude before leveling off. In the case of the 30-deg slat deflection, the computation showed periodic oscillations in the lift coefficient C_L on the order of 0.1–0.4%, indicating flow unsteadiness. It is emphasized that this unsteadiness is self-starting and was not forced. The base flow obtained in this manner was used as the starting state for the time-accurate calculations. A constant nondimensional time step of $\Delta t = 7.726 \times 10^{-5}$ (corresponding to 200 points per period for 40 kHz tone) was used throughout each simulation, except for the refined-grid calculation for which a slightly larger time step of $\Delta t = 1.029 \times 10^{-4}$ was used.

B. Baseline Grid Simulations

For the 30-deg slat deflection, the time-accurate solution settled into a purely periodic state subsequent to the initial transient. The periodic flow fluctuations are mainly concentrated at the slat trailing edge and are due to the vortex shedding at the edge. The fluctuating field was obtained by subtracting the local mean values (determined by averaging the computed solution over a single period of shedding) from the total unsteady solution. The time-averaged Mach contours near the leading edge slat (Fig. 7), clearly display the recirculating zone in the slat cove, the free shear layer originating from the slat cusp, and acceleration of the local flow through the gap. The stagnation points near the slat and main element leading edges are located at the centers of the concentric semicircle contours in Fig. 7. The flowfield interior to the recirculating zone involves extremely low Mach numbers and has closed streamlines. The relatively slow moving recirculating region is separated from the faster moving fluid through the gap by a shear layer that thickens significantly as it curves upward and reattaches to the slat undersurface near the trailing edge. We anticipate this shear layer, along with the recirculation zone, to be an important source of flow unsteadiness and noise generation, albeit at much lower frequencies than the tonal-like hump in the slat spectrum (Fig. 3). The time-averaged Mach contours near

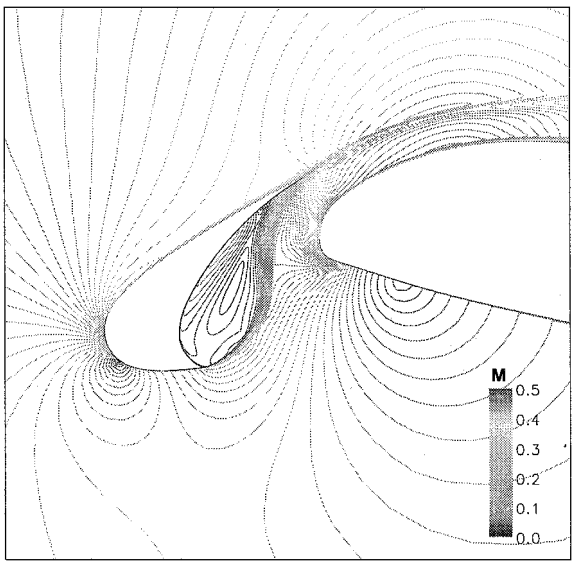

Fig. 7 Time-averaged Mach contours near model leading edge for 30-deg slat deflection.

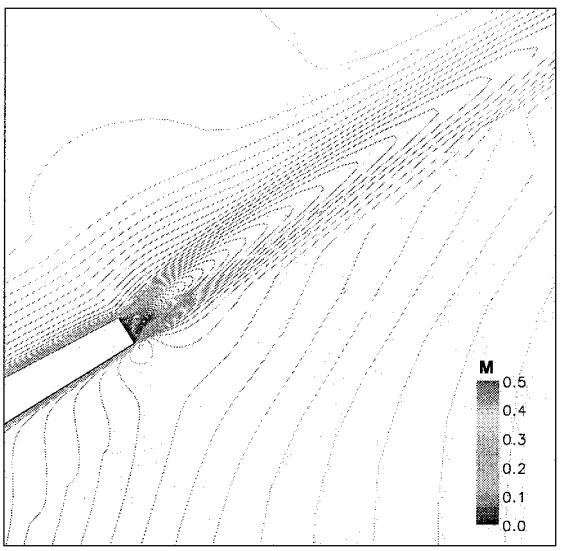

Fig. 8 Time-averaged Mach contours at slat's trailing edge for 30-deg slat deflection.

the slat trailing edge are shown in Fig. 8. The overall characteristics of the trailing wake are displayed. Notable are the slight upward deflection of the wake due to the faster moving gap flow and the presence of a significantly thicker boundary layer on the slat top surface and a much thinner layer on the bottom surface. The low Mach number flow at the trailing edge is confined to a region not much longer than twice the edge height. In fact, close to the edge, the wake possesses a region of reversed flow on its centerline, which suggests the existence of absolute instabilities as the cause behind the vortex shedding phenomenon.

The instantaneous, fluctuating pressure field (nondimensionalized with respect to $1/2\rho_\infty a_\infty^2$) at the slat trailing edge is presented in Fig. 9. The established vortex street is clearly displayed confirming our conjecture regarding the presence of vortex shedding at the trailing edge. Because of the relatively coarse spatial resolution beyond two vortex spacings downstream of the trailing edge, the computed fluctuation field in that region decays rapidly farther downstream. Figure 10 shows the propagating waves and the established wave patterns near the slat's trailing edge and cove areas. The plotted quantity is the fluctuating pressure field within an amplitude range of ± 0.002. Of particular significance is the reflection of the wave at the leading edge of the main element, which results in a very distinct interference pattern across the gap and in the cove area (Fig. 11). As seen from the patterns in Fig. 11, approximately

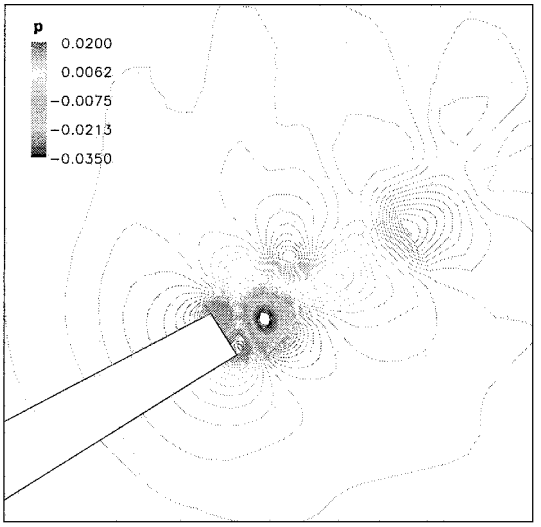

Fig. 9 Instantaneous fluctuating pressure field at slat's trailing edge displaying vortex shedding; slat deflection is 30 deg.

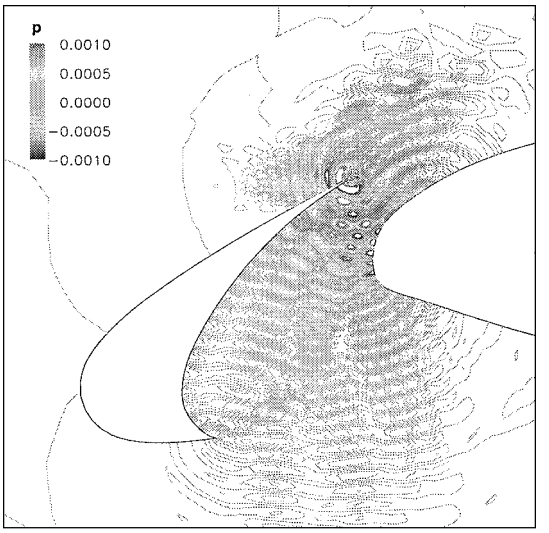

Fig. 12 Fluctuating pressure field showing wave patterns and downward wave propagation in opening between slat and main element; slat deflection is 30 deg.

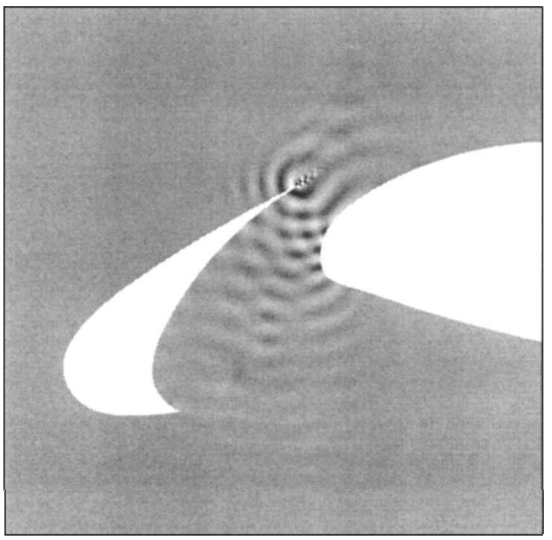

Fig. 10 Instantaneous fluctuating pressure field near leading edge displaying wave propagation; slat deflection is 30 deg.

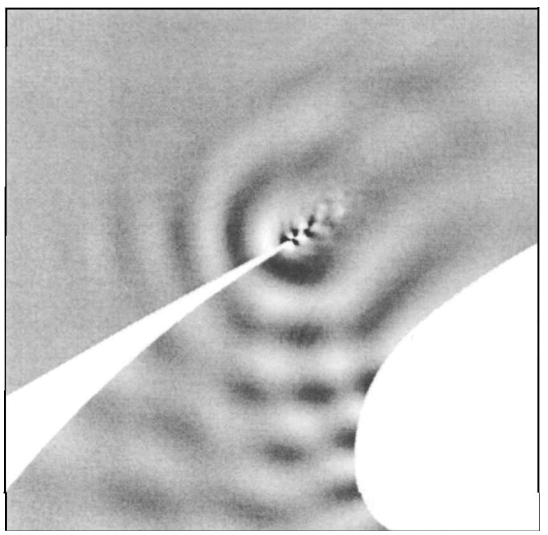

Fig. 11 Instantaneous fluctuating pressure field showing established wave patterns at trailing edge and gap region; slat deflection is 30 deg.

two acoustic wavelengths span the gap distance. This observation raises an important question as to whether a feedback mechanism is operative in the gap. If operative, a feedback mechanism certainly would play an important role in either selecting or influencing the shedding frequency. Unfortunately, we have not had the opportunity to either confirm or refute the presence of feedback mechanism through additional computational experiments. However, during the LTPT experiment, the gap and overhang were changed over a limited range, and no appreciable shift in the high-frequency peak occurred. In addition, examination of the experimental data at a higher Mach number ($M = 0.3$) confirmed the occurrence of the high-frequency hump at a fixed Strouhal number. These observations confirm the belief that the hump is, indeed, caused by some hydrodynamic phenomena (such as shedding) and not by an acoustic resonance mechanism. The downward propagation of the waves through the opening between the slat and the main element is better seen in Fig. 12. Figure 12 indicates that these waves, as they propagate downward, are slightly redirected in the downstream direction by the geometry of the opening.

At this time, a word of caution with regard to the amplitude and directivity of the captured waves is warranted. The present flow solver provides second-order accuracy in both time and space. To capture an acoustic wave, particularly at distances away from the source, higher-order methods are highly desirable. In the present calculations, dissipation and dispersion errors exist due to the lower-order accuracy of the flow solver. However, the objective of the present computations is not to predict the far-field acoustics, but to capture any near-field aerodynamic phenomena that are responsible for the measured peak in the noise spectrum. Given our extremely fine resolution near the trailing edge and the cove area, we believe that the dissipation and dispersion errors will not have any influence on the conclusion drawn herein. In a separate study, Singer et al.[23] used an acoustic analogy to compute the far-field acoustics from the time-history data of the present calculations. The agreement between their computed far-field acoustics and the acoustic array measurements reinforces that the current computations predict the near-field flow dynamics with sufficient accuracy.

The nondimensional unsteady pressure signal on the lower sharp corner at the slat trailing edge is plotted in Fig. 13. The purely periodic nature of the vortex shedding is clearly shown. Fourier analysis of the pressure signal at this and nearby locations indicates a shedding frequency of ≈ 45 kHz. This shedding frequency is within the range of the measured frequencies of the hump shown in Fig. 3.

Having verified the presence of vortex shedding and the likelihood of its accounting for the high-frequency hump in the measured acoustic spectrum, additional simulations were carried out to check if the shedding phenomenon would also explain some of the measured trends (Figs. 3 and 4) in the acoustic spectrum for the

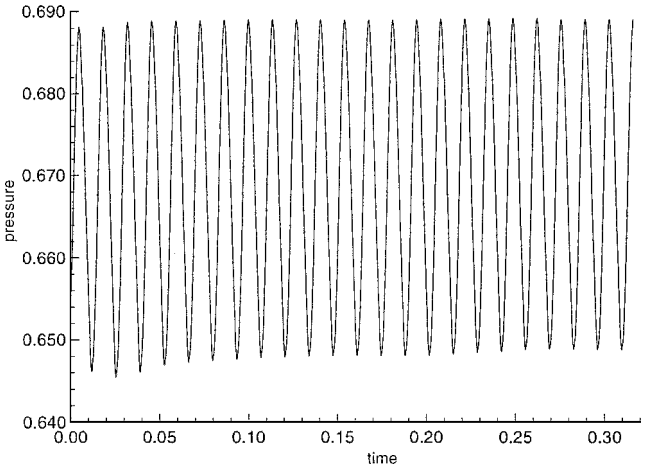

Fig. 13 Periodic nature of nondimensional unsteady pressure signal on lower corner at slat trailing edge; slat deflection is 30 deg.

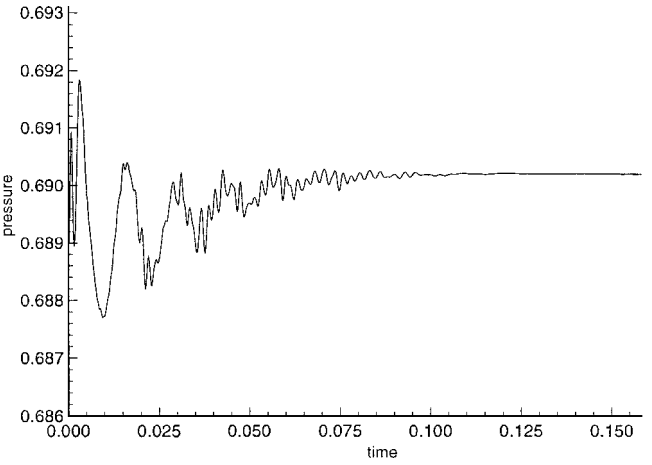

Fig. 14 Nondimensional pressure signal on lower sharp corner at slat trailing edge showing loss of flow unsteadiness; slat deflection is 20 deg.

high-amplitude peak. As a first step, the slat deflection angle was changed to 20 deg (keeping grid topology, number of points, and clustering the same), and the computations were repeated in a steady mode to obtain the starting solution for the unsteady calculations. Once again, the computations showed periodic oscillations in the lift coefficient C_L on the order of 0.02–0.04% (which is an order of magnitude smaller than those present in the 30-deg slat deflection case), suggesting possible flow unsteadiness. For this lower deflection angle, however, the time-accurate computed solution reveals no vortex shedding at the slat trailing edge or any other form of flow unsteadiness in the slat vicinity. Figure 14 shows the unsteady pressure at the trailing-edge lower sharp corner for the 20-deg deflection. The signal indicates that, although initially some form of periodic flow is being established, the unsteadiness levels are considerably weaker than the 30-deg deflection case and are eventually damped out by the flow solver. This behavior is fully corroborated by the measurements at the lower slat deflection, which showed that the hump at high frequencies either diminished significantly or was absent altogether. The steady Mach contours for the 20-deg slat deflection show an overall flow pattern that is very similar to the 30-deg case shown in Fig. 7. In the present case, however, the shear layer reattachment location on the slat bottom surface is closer to the trailing edge. In addition, the Mach contours at the trailing edge indicate a wake that is deflected upward even more and a boundary layer on the top surface that is much thicker when compared to the 30-deg slat configuration.

The effect of lowering the Reynolds number on the vortex shedding mechanism was simulated by repeating the computation for $Re = 2.4 \times 10^6$. Our reason for choosing a Reynolds number lower

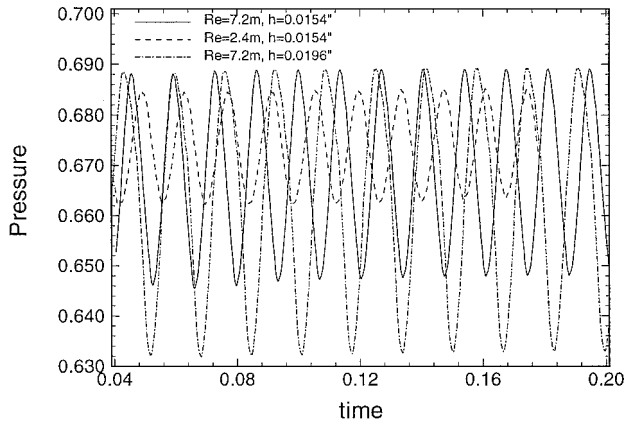

Fig. 15 Nondimensional time-dependent pressure signal on lower corner of slat trailing edge; slat deflection is 30 deg.

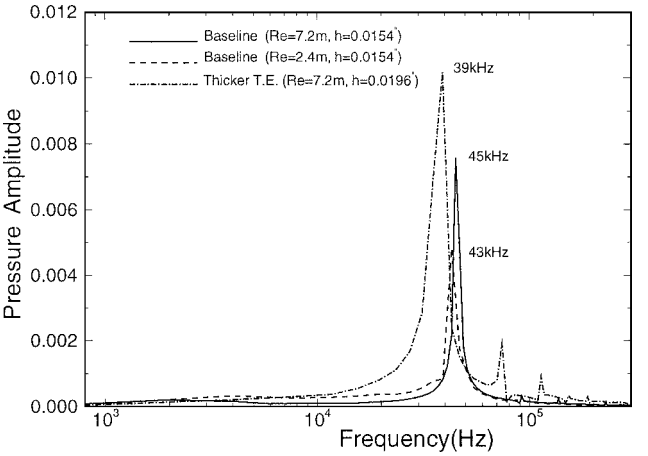

Fig. 16 FFT of time records shown in Fig. 15 revealing shedding frequency; slat deflection is 30 deg.

than 3.6×10^6 was out of concern that the spread between 7.2×10^6 and 3.6×10^6 might not have produced noticeable trends computationally. In hindsight and with the computed results at hand, however, we firmly believe that use of $Re = 3.6 \times 10^6$ would have also provided the anticipated trends. Figure 15 shows a comparison between the unsteady pressure signals at the lower sharp corner of the slat trailing edge for the two Reynolds numbers. The baseline signal is shown by a solid line, whereas the dashed line indicates the signal obtained for $Re = 2.4 \times 10^6$. The organized periodic nature of the record clearly shows that the vortex shedding process remains intact at this lower Reynolds number. On the other hand, there is nearly a 50% reduction in the amplitude of the signal relative to the corresponding amplitude for $Re = 7.2 \times 10^6$. A fast Fourier transform (FFT) of the time record (Fig. 16) revealed a shedding frequency of $\approx$43 kHz as opposed to 45 kHz at $Re = 7.2 \times 10^6$. The reduction in amplitude and the shift to a lower shedding frequency with decreasing Reynolds number are consistent with the measured trends in the high-frequency peak from the slat acoustic spectra (Fig. 3) described in Sec. I.

Measurements of the trailing-edge thickness following the completion of the experiment (and the baseline simulation described earlier) revealed that the EET slat trailing edge was actually thicker than the design value of $h = 0.0154$ in. (0.39 mm). Therefore, the baseline simulation ($Re = 7.2 \times 10^6$, 30-deg slat deflection) was repeated using the measured thickness of $h = 0.0196$ in. (0.5 mm). The additional thickness was added gradually along the chord and only to the slat top surface to keep the gap value identical to that in the earlier runs. Care was taken to ensure that the slat surface remained smooth, with a continuous slope and curvature distribution throughout. The unsteady pressure signal at the bottom corner of the thicker trailing edge ($h = 0.0196$ in.) is plotted in Fig. 15 as a dashed–dotted line. For the thicker edge, the shedding process

is stronger, as evidenced by a 30% increase in the amplitude of the fluctuating pressure. A Fourier transform of the time record is presented in Fig. 16 (dashed–dotted line). As expected, increasing the trailing-edge thickness lowers the shedding frequency to a value of ≈ 39 kHz. Note, however, that although the edge height was increased by 27.3%, the shedding frequency has reduced only by 13.3%. This suggests that the nondimensional frequency (Strouhal number, $Sr = fh/U$, where f is the shedding frequency and U is a reference velocity) may depend on additional length scales besides the geometrical length scale h. Brooks et al.[24] in their extensive study of trailing-edge bluntness for symmetric airfoils at zero angle of attack found a reasonable correlation between the peak Strouhal number and the nondimensional scale h/δ^*, where δ^* is the boundary-layer displacement thickness at the trailing edge. (This correlation was first suggested by Blake[25] for flat plates with blunt trailing edges.) However, difficulties arise when one tries to apply the correlation to the present high-lift flowfield. Given the widely different values of displacement thicknesses on the suction and pressure sides of the slat (see Fig. 8), the proper choice of δ^* becomes problematic. Brooks et al.[24] have suggested using an averaged form of δ^*. A similar complication is encountered during the selection of the appropriate reference velocity U. An alternative length scale, suggested by Hammond and Redekopp,[26] is the combination of the edge height plus the displacement thicknesses. Probing of the computational fluid dynamics (CFD) data suggests this combination to be a more viable scale than an averaged value of δ^*; nonetheless, both approaches fall short of predicting the correct falloff in the shedding frequency. Therefore, additional work is necessary to determine the proper scalings and correlation for the vortex shedding process.

C. Vortex Shedding Process

To explain the loss of vortex shedding at lower slat deflections, we resort to previous theoretical investigations. In his analytical study of flow past a flat plate with blunt trailing edge, Koch[27] postulated that the self-excited vortex shedding process is governed by a resonancelike mechanism, which is associated with a region of locally absolute instability. The shedding frequency is determined by the distance in the wake where transition from absolute to convective instability occurs. Through a parametric study, Koch[27] found that symmetry of the wake plays a prominent role in determining the stability characteristics of the wake. For asymmetrical wakes, a limiting asymmetry seems to exist beyond which no region of absolute instability can be found (loss of shedding) and only convective instabilities are possible. Applying direct numerical simulation to the same geometry, Hammond and Redekopp[26] have confirmed Koch's analysis[27] and clearly establish the link between vortex shedding and the wake global instability characteristics. Readers unfamiliar with the field of hydrodynamic stability are referred to Huerre and Monkewitz[28] for a thorough overview of global instabilities, in general.

Our extensive postprocessing of the time-averaged solutions tends to support the earlier analytical studies. For the case of 30-deg slat deflection, vertical cuts of the streamwise velocity show the wake to possess a region of strong reversed flow on its centerline. The backflow magnitude gradually diminishes in the downstream direction, and in two to three trailing-edge thicknesses downstream of the edge, the wake becomes unidirectional. Although it is tilted upward, the velocity cuts show the wake to be remarkably close to being symmetrical with the bottom stream being slightly stronger. The cited features tend to support a region of absolute instability, which is a necessary condition for establishment of vortex shedding.

In contrast, similar cuts through the averaged velocity field show that the 20-deg slat deflection produces a wake that is markedly different than the 30-deg case. At lower slat deflection, the reverse flow on the wake centerline becomes weaker in magnitude and shorter in streamwise extent. Because of the strong upward tilting of the wake, the bottom stream dominates and leads to a highly asymmetrical wake. These differences will tend to diminish and possibly even eliminate the region of absolute instability, thereby causing either reduction of the amplitude of the vortex shedding process or preventing it from being established.

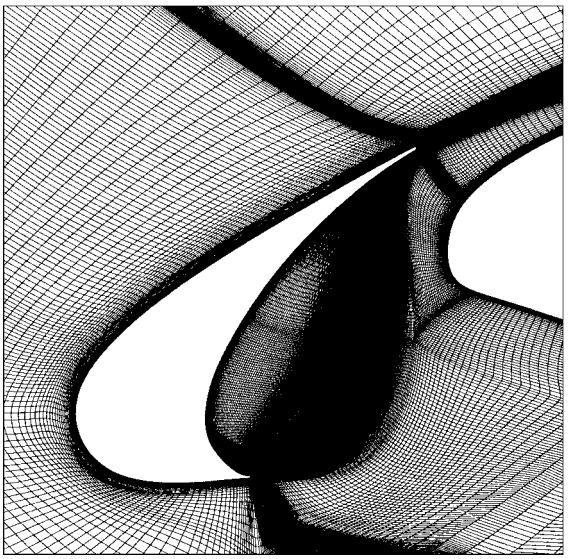

Fig. 17 Fine grid distribution in vicinity of slat; every other point is shown.

D. Refined-Grid Simulation

As is often the case with complex unsteady flow calculations, our simulations have followed an evolutionary path. Although the initial goals of the simulations were modest in nature, as a deeper understanding of the underlying local flow physics emerged, provisions were made to accommodate finer details of the slat geometry and to provide better resolution. The accompanying acoustic analyses (described by Singer et al.[23]) highlighted some of the shortcomings of the initial Reynolds-averaged Navier–Stokes (RANS) simulations, in particular pointing to the slat top surface and cove area as two of the regions requiring better grid resolution. In addition, the slat cusp was also treated as being blunt rather than sharp to match the tested model. The cusp was made 0.01 in. (0.25 mm) thick, which is half the trailing edge height.

The refined-grid distribution in the vicinity of the slat is shown in Fig. 17. The new grid has 21 blocks for a total of 433,000 nodes. Notice that, in comparison with the original distribution (Fig. 5), the new grid has significantly better resolution almost everywhere (in the vicinity of the leading-edge slat), yielding a minimum resolution of 12–14 points per acoustic wavelength based on the vortex shedding frequency. In Fig. 17, note the heavy concentration of the points at the cusp, which were added to provide a resolution similar to that of the trailing edge. The distribution of the nodes in the shear layer (cove) region is extremely fine, providing close to 25 points per acoustic wavelength. We expect this grid to be fine enough to capture the primary mode of instability of the shear layer, if one exists. As indicated earlier, for the larger grid, a time-accurate simulation was conducted using a $\Delta t = 1.029 \times 10^{-4}$, which is $\frac{4}{3}$ of the original time step. We chose a larger Δt to strike a balance between the temporal resolution need of the high-frequency vortex shedding and generation of a sufficiently long time record to search for low-frequency shear layer instabilities. The flow conditions were the same as the baseline case with $Re = 7.2 \times 10^6$, $M = 0.2$, and $h = 0.0196$ in. (0.5 mm).

The amplitude of unsteady pressure signal at the lower corner of the slat trailing edge was found to be 10–15% lower than that obtained with the original grid (Fig. 18). A Fourier transform of the time-dependent signal produced a shedding frequency of 37 kHz vs 39 kHz based on the original solution for a sharp cusp. To ensure that the larger time step employed was not responsible for this loss of amplitude and shift in frequency, the computation was repeated for a few shedding cycles using the original smaller time step. The results were virtually identical to those obtained with the larger Δt, which suggest that the small difference in amplitude and frequency are likely to have been caused by the thick cusp and, possibly, by the grid modifications accompanying this change in geometry.

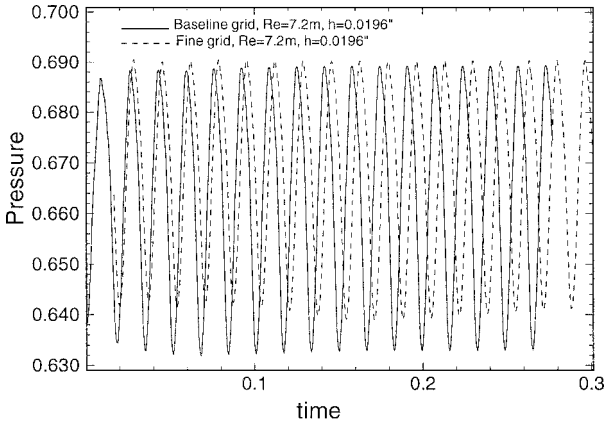

Fig. 18 Nondimensional time-dependent pressure signal on lower corner of slat trailing edge; slat deflection is 30 deg.

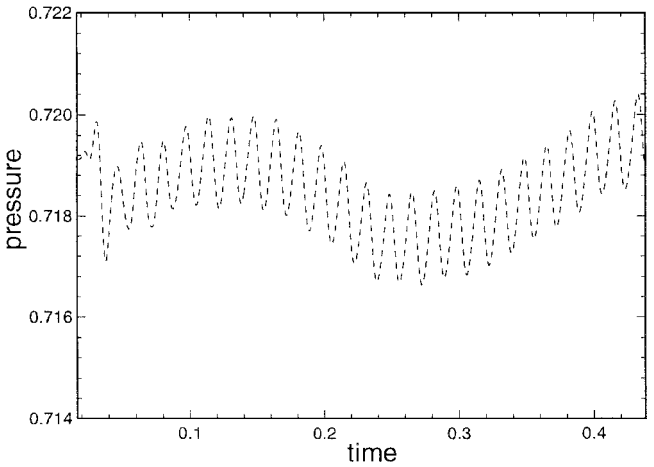

Fig. 19 Nondimensional unsteady pressure signal in shear layer near reattachment point; fine-grid solution with slat deflection of 30 deg and $h = 0.0196$ in. (0.5 mm).

A closer scrutiny of the computed result revealed the presence of relatively weak vortex shedding at the cusp. However, this weak vortex shedding does not seem to translate into an acoustic source, but the role of the cusp flow in triggering, exciting, or enhancing the shear layer instabilities remains an open question. The unsteady pressure signal in the shear layer close to its reattachment location is presented in Fig. 19. The time record shows a low-frequency oscillation in addition to the typical trailing-edge high-frequency shedding signal. This low-frequency oscillation confirms one of our original suspicions that the shear layer is another source of flow unsteadiness and, thus, a potential noise source. Recall that no external forcing was applied in the simulation and that the shear layer unsteadiness is self-starting. A Fourier transform of the pressure record and those from other locations in the shear layer indicate the lower frequency to be in the vicinity of 3 kHz. Unfortunately, as can be seen in Fig. 19, the generated time record is of insufficient length to pinpoint the exact frequency. The computed low-frequency feature is in the proper range of the slat tonal frequencies measured by Dobrzynski et al.[3]

The wave patterns in the vicinity of the slat are shown in Fig. 20. The overall patterns are similar to the less resolved case presented in Fig. 10. However, with the added resolution, wave propagation on the slat top surface is fully captured. Also noticeable in Fig. 20 is the redirection and scattering of the acoustic waves near the slat cusp, which lead to cylindrical wave patterns that move away from the cusp. Currently, we are in the process of analyzing the time-dependent flowfield to better understand the underlying source of unsteadiness in the shear layer. In addition, the refined-grid simulation is being extended to provide a longer time record to confirm the longevity of the low-frequency oscillations noted earlier.

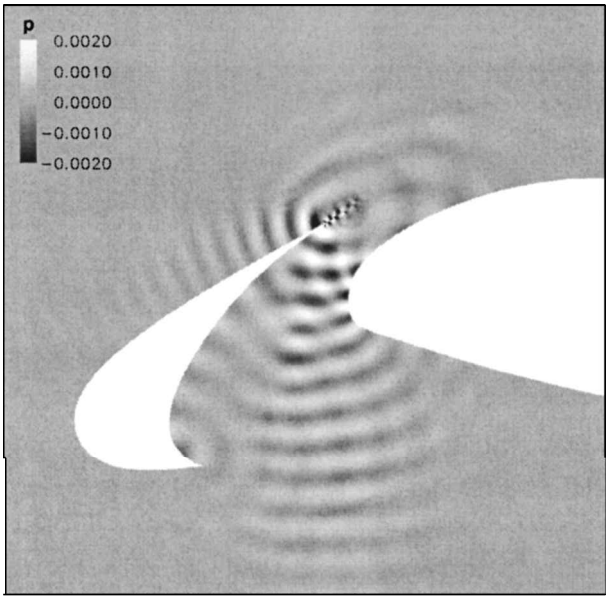

Fig. 20 Instantaneous fluctuating pressure field near leading edge displaying established wave patterns; fine grid solution with slat deflection of 30 deg and $h = 0.0196$ in. (0.5 mm).

IV. Conclusions

Time-accurate RANS simulations were carried out to study the high-lift flowfield on an EET configuration, with a particular emphasis on the unsteady flowfield near a blunt slat trailing edge. The computational resolution was adequate to capture the details of the local flowfield that are relevant to airframe noise generation. Analysis of the unsteady data revealed the presence of strong vortex shedding behind the blunt edge, which leads to generation of tonal noise. The vortex shedding process (which occurs only at a sufficiently high slat deflection) corresponds to a frequency range of 37–45 kHz, depending on the magnitude of the edge bluntness and flow Reynolds number. Although occurrence of shedding does not necessarily translate into the measured (far-field) tonelike feature, the computed near-field acoustics is strongly suggestive of this being the case. Direct computation of the far-field acoustics with the CFD solver employed would have been impractical. However, as shown by Singer et al.,[23] the far-field radiation can still be determined using the computed CFD solution in the framework of an acoustic analogy. Their study establishes quite convincingly the link between the trailing-edge shedding and the observed hump in the spectrum. The computed shedding frequencies are in good agreement with the measured spectral peaks from the LTPT experiment at NASA Langley Research Center. The findings confirm our conjecture that vortex shedding is responsible for the strong high-frequency hump in the measured acoustic spectra of a 30-deg deflected slat. The generated acoustic waves propagate downward through the slat gap and cove areas, directed slightly toward the downstream direction. A finely resolved solution indicates the presence of additional, low-frequency oscillations in the free shear layer originating at the slat cusp; the aeroacoustic significance of the shear layer oscillations and their (possible) interaction with other sources of slat unsteadiness is currently under investigation.

Acknowledgments

This paper is dedicated to the memory of Michele G. Macaraeg (1956–1999), a friend and a visionary, whose tireless efforts helped enable several breakthroughs in the computational modeling of airframe noise sources. Her ardent leadership of the airframe noise program at NASA Langley Research Center will be long remembered.

This work was sponsored by NASA Contract NAS1-20102 (Lockheed Martin Corporation Subcontract RT46324). Most of the computations were performed on the C-90 Cray computers provided by the National Aerodynamic Simulation Facility. The authors would like to thank the various members of the Airframe

Noise Team at NASA Langley Research Center, in particular, Craig Streett, Michele Macaraeg, and Thomas Brooks, for stimulating and helpful discussions related to this work. The contribution of Michael Wiese of Computer Science Corporation, who generated the initial grid and all of the required modifications thereafter, is also greatly appreciated.

References

[1]Meadows, K. R., Brooks, T. F., Humphreys, W. M., Hunter, W. H., and Gerhold, C. H., "Aeroacoustic Measurements of a Wing-Flap Configuration," AIAA Paper 97-1595, 1997.

[2]Hayes, J. A., Horne, W. C., Soderman, P. T., and Bent, P. H., "Airframe Noise Characteristics of a 4.7% Scale DC-10 Model," AIAA Paper 97-1594, 1997.

[3]Dobrzynski, W., Nagakura, K., Gehlhar, B., and Buschbaum, A., "Airframe Noise Studies on Wings with Deployed High-Lift Devices," AIAA Paper 98-2337, 1998.

[4]Davy, R., and Remy, H., "Airframe Noise Characteristics on a 1/11 Scale Airbus Model," AIAA Paper 98-2335, 1998.

[5]Storms, B. L., Ross, J. C., Horne, W. C., Hayes, J. A., Dougherty, R. P., Underbrink, J. R., Scharpf, D. F., and Moriarty, P. J., "An Aeroacoustic Study of an Unswept Wing with a Three-Dimensional High-Lift System," NASA TM-1998-112222, 1998.

[6]Khorrami, M. R., Singer, B. A., and Takallu, M., "Analysis of Flap Side-Edge Flowfield for Identification and Modeling of Possible Noise Sources," Society of Automotive Engineers, Paper 971917, Traverse City, MI, May 1997.

[7]Khorrami, M. R., Singer, B. A., and Radeztsky, R. H., Jr., "Reynolds Averaged Navier–Stokes Computations of a Flap Side-Edge Flow Field," *AIAA Journal*, Vol. 37, No. 1, 1999, pp. 14–22.

[8]Takallu, M. A., and Laflin, K. R., "Reynolds-Averaged Navier–Stokes Simulations of Two Partial-Span Flap Wing Experiments," AIAA Paper 98-0701, 1998.

[9]Radeztsky, R. H., Singer, B. A., and Khorrami, M. R., "Detailed Measurements of a Flap Side-Edge Flowfield," AIAA Paper 98-0700, 1998.

[10]Khorrami, M. R., and Singer, B. A., "Stability Analysis for Noise-Source Modeling of a Part-Span Flap," *AIAA Journal*, Vol. 37, No. 10, 1999, pp. 1206–1212.

[11]Streett, C. L., "Numerical Simulation of Fluctuations Leading to Noise in a Flap-Edge Flowfield," AIAA Paper 98-0628, 1998.

[12]Macaraeg, M. G., "Fundamental Investigations of Airframe Noise," AIAA Paper 98-2224, 1998.

[13]Thomas, J., Krist, S., and Anderson, W., "Navier–Stokes Computations of Vortical Flows over Low-Aspect-Ratio Wings," *AIAA Journal*, Vol. 28, No. 2, 1990, pp. 205–212.

[14]Roe, P., "Approximate Riemann Solvers, Parameter Vectors, and Difference Schemes," *Journal of Computational Physics*, Vol. 43, 1981, p. 357.

[15]Biedron, R. T., Krist, S. L., Thomas, J. L., and Baysal, O., "Overset Grid Applications at Langley Research Center," Overset Composite Grid Workshop, Research Inst. for Advanced Computer Science, NASA Ames Research Center, CA, May 1992.

[16]Baysal, O., Fouladi, K., Leung, R. W., and Sheftic, J. S., "Interference Flows Past Cylinder–Fin–Sting–Cavity Assemblies," *Journal of Aircraft*, Vol. 29, No. 2, 1992, pp. 194–202.

[17]Fouladi, K., Baysal, O., Newman, J. C., III, "Hybrid Domain Decomposition for Configurations with Multi and Nonsimilar Components," *Proceedings of 5th International Symp. on Domain Decomposition Methods for Partial Differential Equations*, Society for Industrial and Applied Mathematics, Philadelphia, 1991, Chap. 39, pp. 476–484.

[18]Menter, F., "Improved Two-Equation $k-\omega$ Turbulence Models for Aerodynamic Flows," NASA TM 103975, 1992.

[19]Rumsey, C. L., Biedron, R. T., Farassat, F., and Spence, P. L., "Ducted-Fan Engine Acoustic Predictions Using a Navier–Stokes Code," *Journal of Sound and Vibration*, Vol. 213, No. 4, 1998, pp. 643–664.

[20]Rumsey, C. L., Sanetrik, M. D., Biedron, R. T., Melson, N. D., and Parlette, E. B., "Efficiency and Accuracy of Time-Accurate Turbulent Navier–Stokes Computations," *Computers and Fluids*, Vol. 25, No. 2, 1996, pp. 217–236.

[21]Berkman, M. E., Khorrami, M. R., Choudhari, M. M., and Sadowski, S. S., "Investigation of High-Lift Flowfield of an Energy Efficient Transport Wing," *Journal of Aircraft*, Vol. 37, No. 1, 2000, pp. 45–52.

[22]Krist, S. L., Biedron, R. L., and Rumsey, C. L., "CFL3D User's Manual (Version 5.0)," NASA TM-1998-208444, June 1998.

[23]Singer, B. A., Lockard, D. P., Brentner, K. S., Khorrami, M. R., Berkman, M. E., and Choudhari, M., "Computational Aeroacoustic Analysis of Slat Trailing-Edge Flow," AIAA Paper 99-1802, June 1999.

[24]Brooks, T. F., Pope, D. S., and Marcolini, M. A., "Airfoil Self-Noise and Prediction," NASA RP 1218, July 1989.

[25]Blake, W. K., "Aero-Hydroacoustics for Ships," Vol. 2, U.S. Navy, Rept. DTNSRDC-84/010, June 1984.

[26]Hammond, D. A., and Redekopp, L. G., "Global Dynamics of Symmetric and Asymmetric Wakes," *Journal of Fluid Mechanics*, Vol. 331, 1997, pp. 231–260.

[27]Koch, W., "Local Instability Characteristics and Frequency Determination of Self-Excited Wake Flows," *Journal of Sound and Vibration*, Vol. 99, No. 1, 1985, pp. 53–83.

[28]Huerre, P., and Monkewitz, P., "Local and Global Instabilities in Spatially Developing Flows," *Annual Review of Fluid Mechanics*, Vol. 22, 1990, pp. 473–537.

M. Samimy
Associate Editor